RSC Advances

ROYAL SOCIETY OF CHEMISTRY

www.rsc.org/advances

Journal Name

ARTICLE

The thermoelectric performance of anisotropic SnSe Doped with Na

Received 00th January 20xx,
Accepted 00th January 20xx

DOI: 10.1039/x0xx00000x

www.rsc.org/

Hua-Qian Leng,[a,b] Min Zhou,[a*] Jie Zhao,[a,b] Ye-Mao Han,[a,b] Lai-Feng Li[a*]

Lead-free polycrystalline SnSe is a promising thermoelectric compound consisting of earth-abundant elements. However, poor electrical transport property for low intrinsic defect concentration (3×10^{17} cm^{-3}) limits the usage of stoichiometric SnSe compound. In this work, Na_2Se as acceptors was doped into SnSe compound in order to optimize the electrical transport properties, especially to increase the carrier concentration. As a result, the carrier concentrations increased and saturated at about 1.0×10^{19} cm^{-3} for $Na_{0.01}Sn_{0.99}Se$ at 300K. A maximum power factor of 0.48 $mWm^{-1}K^{-2}$ was obtained. And a maximum *zT* value of 0.75 was obtained at 823 K for $Na_{0.01}Sn_{0.99}Se$ along the direction perpendicular to the sintering pressure, which is 25% higher than that (0.6) of the undoped SnSe compound.

Introduction

Thermoelectric material is a kind of material that could convert heat to electricity directly, or vice versa. Devices made by thermoelectric material have advantages of no moving parts, quiet operation, low environmental impact and high reliability. The performance of thermoelectric materials can be evaluated by the dimensionless figure of merit, $zT = S^2\sigma T/\kappa$, where S, σ, κ, T are the Seebeck coefficient, the electrical conductivity, the thermal conductivity and the absolute temperature, respectively[1]. Continuous efforts have been invested into optimizing thermoelectric performance, for example, phonon engineering[2,3], band engineering[4-6] and point defect engineering[7,8] etc. Binary bismuth and lead chalcogenides such as Bi_2Te_3, PbTe, and their solid solutions have been intensively studied with above optimizing methods for thermoelectric applications[9,10,11]. However, for those thermoelectric materials, in spite of high *zT* values (>1) obtained, widespread application is restricted for toxic Pb and costly Te, which make SnSe obtain more attention as a potential alternative.

Currently, SnSe crystal draws considerable attentions for its extremely high *zT* values (2.6 and 2.3 at 950 K along the b and c axes, respectively[12]). The extremely high *zT* values is mainly attributed to its ultralow lattice thermal conductivity for the distinctive anharmonic structure in SnSe[12]. SnSe has a layered orthorhombic crystal structure, resembling a distorted NaCl rock-salt structure (shown in Figure 1). Along the b-c plane, two-atom-thick SnSe slabs creating a zig-zag accordion-like projection along the b axis spread within the plane of the slabs. Those two-atom-thick SnSe slabs were linked with weaker Sn-Se bonding along the a-axis direction, and contributed the easy cleavage along (l00) plane[13]. The distinctive structure results in its outstanding anisotropy. For single crystal, weak bonding between Sn-Se in SnSe slabs leads to poor mechanical properties. And compared with polycrystalline, preparation technology of single crystal is complicated. These all contribute to the study of polycrystalline SnSe. The low intrinsic thermal conductivity values (0.3-0.8 W $m^{-1}K^{-2}$) and low intrinsic carrier concentration value (3×10^{17} cm^{-3}) of undoped polycrystalline SnSe were reconfirmed at room temperature[14]. One feasible solution toward the poor electrical transport property is increasing the carrier concentrations. Various candidates (Na, Ag, Sr, In, Pb and Tl) as dopants were attempted[15], but only Na and Ag seem to be able to dope and increase the carrier concentrations. Na-doping in polycrystalline SnSe increases carrier concentrations but decreases the band gap. In general, bipolar thermal transport is controlled by the minority carrier partial electrical conductivity and band gap for extrinsic cases[22]. As a result, the decreasing band gap and the minority carrier partial electrical conductivity compensate each other for thermal conductivity, especially for bipolar conduction.

In this work, we synthesized a sequence of p-type $Na_xSn_{1-x}Se$ (x=0.0025-0.02) polycrystalline by melting and Spark Plasma Sintering (SPS) methods. And the orientation degree and the transport properties in different directions were investigated for the outstanding anisotropy of the single crystal SnSe. A maximum *zT* value of 0.75 was observed for $Na_{0.01}Sn_{0.99}Se$ in perpendicular to the pressing direction at 823 K. In parallel to the pressing direction, a maximum *zT* value of 0.61 was obtained at 823 K.

[a] Key Laboratory of Technologies in Space Cryogenic Propellants, Technical Institute of Physics and Chemistry, Chinese Academy of Sciences, Beijing, China.
[b] University of Chinese Academy of Sciences, Beijing, China.
Corresponding Author:
Min Zhou mzhou@mail.ipc.ac.cn Laifeng Li laifengli@mail.ipc.ac.cn
Electronic Supplementary Information (ESI) available: [1. The calculated Hall mobility in this work as a function of Ag content (x) at 300 K. 2. The experimental results and theoretical method of indirect-bandgap calculations. 3. The thermal stability of the polycrystalline materials.]
See DOI: 10.1039/x0xx00000x

Results and discussion

Figure 2(a) shows the X-ray diffraction (XRD) patterns of $Na_xSn_{1-x}Se$(x=0, 0.0025, 0.005, 0.0075, 0.01, 0.02) powders grounded from ingots. All diffraction peaks can be well indexed to the

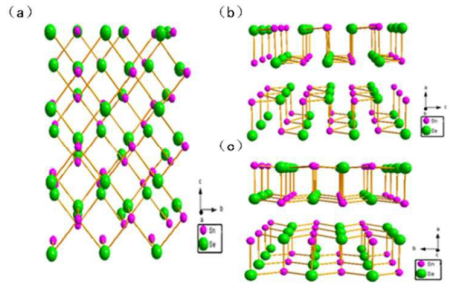

Figure 1 (a) Crystal structure along the a axis: magenta, Sn atoms; green, Se atoms. (b) Structure along the b axis. (c) Structure along the c axis.

orthorhombic SnSe phase ((PDF#48-1224) low temperature phase, Cmcm), suggesting the formation of single phase SnSe-based solid solutions. No impurity phase is observed for all samples. The X-ray diffraction (XRD) patterns of the $Na_xSn_{1-x}Se$ was refined by Retiveld full file fitting method, and the lattice parameter (a=11.5147 Å, b=4.159 Å, c=4.451 Å) was calculated by using general structure analysis system (GSAS), which was in accordance with literature[15]. Figure 2(b) is the XRD patterns of the polycrystalline SnSe bulk in both perpendicular and parallel to the pressing direction. Different from the standard card (PDF#48-1224), the strongest peak in the direction parallel to pressing was observed in (400) peak not in (111) peak. However, in another measuring direction, the XRD with the strongest peak in (111) matches well with the standard card (PDF#48-1224). Those all suggest that the (400) peak in perpendicular to the pressing direction possesses some preferred orientation. The orientation degree of polycrystalline in (hkl) planes can be evaluated by orientation factor (termed as *F*) along the corresponding direction. The orientation factor of the c- planes (h00) was calculated with the Lotgering method by the following equations[16]:

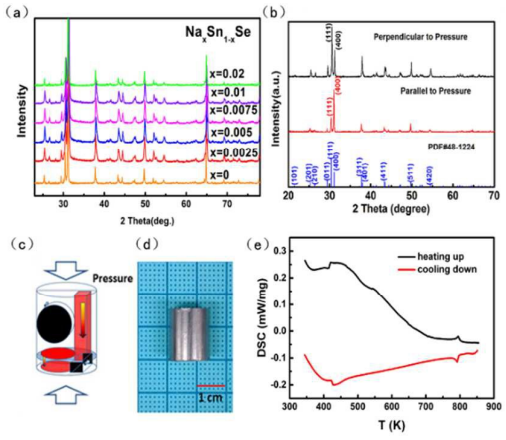

Figure 2 (a) XRD patterns of NaxSn1-xSe (x=0, 0.0025, 0.005, 0.0075, 0.01, 0.02) powders grounded from ingots. (b) XRD patterns of SnSe bulks sintered by SPS in both parallel and perpendicular to the pressing direction. (c) The sample cut direction for measurements along different directions. (d) A photograph of a bulk sample sintered by SPS. (e) Differential Scanning Calorimeter (DSC) for Na0.01Sn0.99Se. The exothermal (endothermal) peak is observed at 803 K.

$$F = \frac{P - P_0}{1 - P_0}$$

$$P_0 = \frac{I_0(h00)}{\Sigma I_0(hkl)} \quad (1)$$

$$P = \frac{I(h00)}{\Sigma I(hkl)} \quad (2)$$

(3)

Where P and P_0 are the ratios of the integrated intensities of all (h00) planes to those of all (hkl) planes for preferentially and randomly oriented samples, respectively. The orientation factor (F=0.32) in parallel to the pressing direction is much higher than that (F=0) in perpendicular to the pressing direction, which is coincide with the observed results (shown in Figure 2(b)). This could be attributed to the cleavage in (h00) plane. Under the sintering pressure, the cleavage plane tends

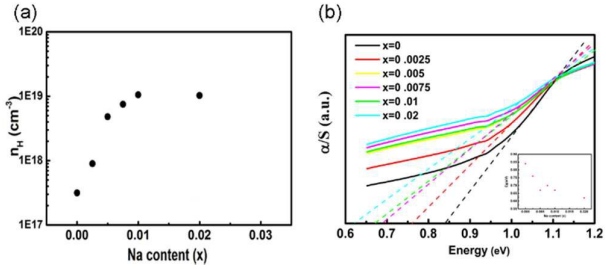

to the direction perpendicular to the pressing direction, which performs a highly oriented degree in parallel to the pressing direction, namely a stronger (400) peak in parallel to the pressing direction.

Figure 3 (a) Hall carrier concentration as function of Na content at 300K. (b) UV-Vis-NIR spectrums result for $Na_xSn_{1-x}Se$ (x=0, 0.0025, 0.005, 0.0075, 0.01, 0.02) with the measured band gap values shown in the inset, where α, S and energy are the absorption coefficient, scattering coefficients and photon energy, respectively.

Figure 2(e) shows the DSC of the Na-doped $Na_{0.01}Sn_{0.99}Se$ compound. The exothermal (endothermal) peak of $Na_{0.01}Sn_{0.99}Se$ is observed around 800 K, indicating the phase transition from the Pnma (D_{2h}^{16}) phase to the Cmcm (D_{2h}^{17}) phase. The temperature of phase transition matches well with the previous reports by Zhao et al[12].

Figure 3(a) shows the Hall carrier concentration of $Na_xSn_{1-x}Se$ as function of Na content at 300K. The measured Hall carrier concentration of the undoped SnSe is around 3×10^{17} cm^{-3} at 300 K, which is consistent with the prior report[15]. With Na doping, the carrier concentration increases and saturates at about 1.0×10^{19} cm^{-3} for $Na_{0.01}Sn_{0.99}Se$. Fig. 3(b) shows UV-Vis-NIR spectrums results for all $Na_xSn_{1-x}Se$. The band gap of the undoped SnSe was determined to be 0.84 eV, which matches the past literature well[12]. With increasing Na, the band gap of the $Na_xSn_{1-x}Se$ shows decreasing trends.

The electrical transport parameters of $Na_xSn_{1-x}Se$ compounds in both parallel and perpendicular to the pressing direction are shown in Fig. 4. The electrical conductivity of undoped SnSe keeps a typical semiconducting behavior, which remains a low level below 573k, then rapidly increases with the temperature. It is noteworthy that the electrical conductivity of $Na_{0.0025}Sn_{0.9975}Se$ shows a similar trend to that of SnSe, which is related to the low carrier concentration (shown in Figure 3(a)). For the $Na_xSn_{1-x}Se$ (x>0.0025), the electrical conductivity decreases and turns to increase over 673 K with temperature indicating the thermal excitation of the intrinsic semiconducting carriers. The significant increase of the electrical conductivity is attributed to the improvement of the carrier concentrations. With Na doping, the carrier concentration increases from 3×10^{17} cm^{-3} to 1.0×10^{19} cm^{-3}. A maximum electrical conductivity of 49.55 $S\bullet cm^{-1}$ is obtained for $Na_{0.01}Sn_{0.99}Se$ at 823K in perpendicular to the pressing direction.

At the same temperature, the electrical conductivity in perpendicular to pressing direction is higher than that in another measuring direction, (as shown in Figure 3(b)). The difference in both measuring directions for electrical conductivity mainly comes from the outstanding anisotropy of the effective mass. Based on the Fermi surface shape, the effective mass possesses the highest value along a-axis direction (corresponding to perpendicular to the SnSe layers) meaning a higher effective mass in parallel to pressing

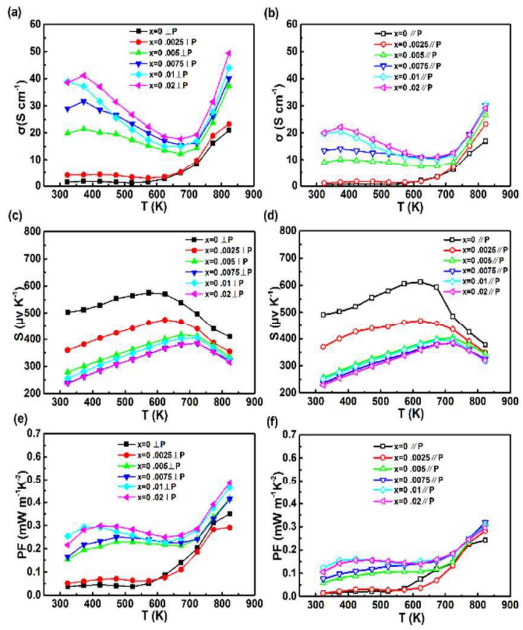

direction[17].High

Figure 4 the electrical transport properties as a function of temperature for $Na_xSn_{1-x}Se$ (x=0, 0.0025, 0.005, 0.0075, 0.01, 0.02) measured along perpendicular and parallel to the sintering pressure. (a)(b), the electrical conductivity. (c)(d), the Seebeck coefficient. (e)(f), the power factor.

effective band mass results in a low mobility. Because the mobility ($\mu = \tau e / m^*$) is inversely proportional to inertial mass

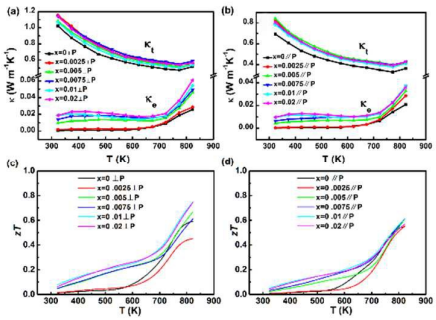

when the carriers are predominantly scattered by phonons. And the scattering time τ decreases with m_b^* . Simultaneously, overall density of states (DOS) effective mass ($m_d^* = N_V^{2/3} m_b^*$) is proportional to effective band mass [5].

All Seebeck coefficient is positive in the measured temperature range indicating *p*-type electrical transport property. For undoped SnSe, Seebeck coefficient starts to decrease over 573K

Figure 5 The thermal transport properties as a function of temperature for $Na_xSn_{1-x}Se$ (x=0, 0.0025, 0.005, 0.0075, 0.01, 0.02) measured along perpendicular and parallel to the sintering pressure. (a)(b), the total thermal conductivity (κ_t) and electronic thermal conductivity (κ_e). (c)(d), the *zT*.

for the thermal excitation corresponding to the change in electrical conductivity. With increasing Na, the temperature of the maximum Seebeck coefficient demonstrates an increasing trend while the band gap gradually decreases. This mainly results from the elevation in carrier concentrations. Different from the electrical conductivity, the Seebeck coefficient of $Na_xSn_{1-x}Se$ shows scarcely difference in both parallel and perpendicular to the pressing direction.

Figure 3(e) and 3(f) show the power factor of $Na_xSn_{1-x}Se$ as function of temperature in both parallel and perpendicular to the pressing direction. The maximum power factor of the undoped SnSe is 0.29 mW $m^{-1}K^{-2}$. With Na doping, the maximum power factor of 0.48 mW $m^{-1}K^{-2}$ is obtained for $Na_{0.02}Sn_{0.98}Se$ at 823K in the direction perpendicular to the sintering pressure, which is 39.58% higher than that for the SnSe. The power factor maximum in parallel to pressing direction is 0.32 mW $m^{-1}K^{-2}$ which is 33.33% lower than that in another measuring direction. The outstanding anisotropy in power factor is observed.

Fig. 5(a) and 5(b) show the temperature dependence of the thermal conductivity of all the samples in both perpendicular and parallel to the sintering pressure. The thermal conductivity of all samples decreases with temperature below 773K due to the increased phonon-scattering. When the temperature is over 773K, a turn happens to the thermal conductivity, which is related to the phase transition from Pnma space group to Cmcm space group at around 800 K (as shown in Figure 2(c)). Derived from the strong anharmonicity in bonding, low temperature Pnma phase SnSe possesses lower thermal conductivity values than high temperature Cmcm phase SnSe[18] . The Pnma phase with a zig-zag geometry structure, like a retractable spring in (l00) plane, is called soft lattice. This "soft" structure slows down heat travelling well. Because the elastic net weaved with the weaker bonding between SnSe

slabs does not transmit vibrations well and restricts the phonon transport[12]. Those above all give rise to low lattice thermal conductivity in ordered crystal structures[19,20,21].

At the same temperature, the thermal conductivity with different Na contents varies less than 15% among all compositions ranging from 0% to 2%. This results from that the improvement of thermal conductivity is mainly attributed to the phonon conduction component, not the electronic thermal conductivity. For $Na_xSn_{1-x}Se$ (x>0), the higher phonon conduction could be related to the fluctuation of soft lattice caused by the change in the strain field which mainly depends on bond polarity. The larger electronegativity difference between cations and anions is, the higher intensity of bond polarity is. The enormous difference between Sn–Se and Na–Se (the electronegativity of Na and Sn are 0.93 and 1.96) could rigidify the soft lattice, which results in a slight improvement in the phonon conduction.

In general, the significant improvement of the carrier concentration tends to contribute to the bipolar thermal conductivity. However, it is interesting that distinctive difference in thermal conductivity is not observed between SnSe and Na-doped SnSe at high temperature range. The barely difference in the trends of thermal conductivity could be attributed to the drop of gap band (E_g). For a single parabolic band and acoustic phonon scattering (λ = −1/2), bipolar thermal conductivity in semiconductors can be expressed as: [22]

$$\frac{\left(\frac{k_B}{e}\right)^2\left[\frac{E_g}{k_BT}+\frac{2F_1(\xi_P)}{F_0(\xi_P)}+\frac{2F_1(\xi_n)}{F_0(\xi_n)}\right]^2 T}{\kappa_b}=\frac{1}{\sigma_n}+\frac{1}{\sigma_p} \qquad (4)$$

Where k_B is the Boltzmann constant, e the free electron charge, ξ the reduce Fermi energy, F_x the Fermi integral of the order of x. Therefore $\xi_n+\xi_p = -E_g/k_BT$, where E_g is the band gap. In general, bipolar thermal transport is controlled by the minority carrier partial electrical conductivity for extrinsic cases[22]. With increasing Na, the band gap of the $Na_xSn_{1-x}Se$ shows a decreasing trend which weakens the effects of the carrier concentration on bipolar thermal conductivity. The thermal conductivity shows anisotropy in different measuring directions.

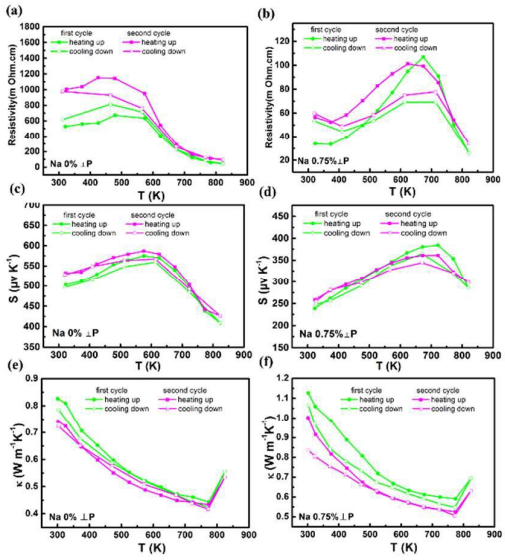

Figure 6 Temperature dependence of (a)(b) electrical conductivity, (c)(d) seebeck coefficient, (e)(f) total thermal conductivity, for sample SnSe and $Na_{0.0075}Sn_{0.9925}Se$ respectively with measurements from room temperature to 823 K (closed green circles squares), then back to room temperature (open green circles), then increased again to 823 K (closed pink squares), and then decreased to room temperature (open pink squares).

Figure 5(c) and 5(d) show the temperature dependence of zT values for $Na_xSn_{1-x}Se$. The zT value of the undoped SnSe increases with temperature and a maximum zT of 0.6 is obtained at 823 K, which is higher than the previous reports[14,15]. The maximum zT value of 0.75 is obtained for $Na_{0.01}Sn_{0.99}Se$ at 823 K in perpendicular to the pressing direction. In parallel to the pressing direction, the maximum zT of 0.61 is obtained for $Na_{0.01}Sn_{0.99}Se$. The enhancement of zT for Na-doped SnSe is mainly attributed to the optimization of electrical transport performance.

Compared with Ag-doped SnSe[15,26], the increase of zT values in both $Na_xSn_{1-x}Se$ and $Ag_xSn_{1-x}Se$ is attributed to the rise of electrical transport properties (shown in ESI). It is worth noting that the extremum values of $Na_xSn_{1-x}Se$ emerge at higher temperature than that of $Ag_xSn_{1-x}Se$ in both resistivity and seebeck coefficient. This could be derived from the effects of different dopants to different extents on band gap.

Experimental

The weighted elemental tin (Sn, 99.999%), Selenium (Se, 99.999%), Na_2Se (99.99%) were loaded into graphite crucible, then loaded into quartz ampoules. The ampoules were evacuated to 7.5×10^{-5} Pa, sealed, and slowly heated up to 1253 K over 12 h, then kept that temperature for 24 h followed by water quench. The obtained ingots were annealed at 973K for 7 days followed by another water quench. The annealed ingots were ground into powders with an agate mortar, the powders were loaded into graphite mould with 13 mm diameter and sintered in Spark Plasma Sintering (SPS) under 50 MPa pressure and 873 K for 5min. The cylinders (Figure 1d) were cut into Bar- and coin-shaped samples (Figure 1c) along different directions for electrical and thermal transport measurements. The parallel (perpendicular) to pressing direction was defined as electrical and thermal properties test direction was parallel (perpendicular) to SPS pressing direction.

The phase composition was analyzed by powder X-ray diffraction (XRD) with X-ray diffract-meter (Cu Kα radiation λ=0.154 nm, Bruker, German). The temperature dependence of electrical conductivity, Seebeck coeffici ent was tested by LSR-3 (Linseis) under static Helium atmosphere. The thermal conductivity was calculated from the relationship $\kappa=\rho C_p\lambda$, the heat capacity value C_p was taken from Chen's work[15], which was calculated from a fitting equation given by Pashinkin et al.[23]and Yamaguchi et al.[24]. The temperature dependence of thermal diffusivities λ was tested by the laser flash method (LFA-457, Netzsch) under flow argon atmosphere. Thermal analysis were carried out by Differential Scanning Calorimeter (DSC404-F3). The Hall coefficient was determined using the Physical Property Measurement System (PPMS-14, Quantum

Design) under the magnetic field of -1T~1T. The ultraviolet-visible-near infrared (UV-Vis-NIR) spectrum was obtained using a Cary 5000 spectrophotometer (Varian, USA) at 300 K. The density ρ of the SPS-sintered samples was measured by the Archimedes' method. The relative density of all the samples is over 97% of the theoretical value (6.18 g/cm^3). The Hall mobility was calculated from the relationship: $\mu_H = \sigma / ne$, where σ is electrical conductivity, *n* is carrier concentration and *e* is electron charge. The K_L was obtained using the Wiedemann-Franz law $K_e = L_0 \sigma T$, $K_L = K - K_e$ .The L_0 is the Lorenz constant (L_0=1.50×10^{-8} V^{2}K^2) for non-degenerate[25].

Conclusions

The polycrystalline Na-doped SnSe compounds were prepared by melting and Spark Plasma Sintering. Upon heating and cooling, compared with the hysteresis of Na-doped SnSe, the polycrystalline SnSe performs relatively stable reproducibility. The $Na_xSn_{1-x}Se$ alloys exhibit anisotropic thermoelectric performance. Na_2Se is an effective acceptor dopants in SnSe compound. With Na doping, the carrier concentration increases from 3×10^{17} cm^{-3} to 1.0×10^{19} cm^{-3}. The maximum *zT* value of 0.75 was obtained for $Na_{0.01}Sn_{0.99}Se$ at 823 K, which is 25% higher than that (0.6) of the undoped SnSe compounds.

Notes and references

1. G. S. Nolas, J. Sharp and J. Goldsmid, *Thermoelectrics: basic principles and new materials developments*, Springer Science & Business Media, 2001.
2. H. Li, X. F. Tang, Q. J. Zhang and C. Uher, *Applied Physics Letters*, 2009, 94, 102114.
3. X. W. Wang, H. Lee, Y. C. Lan, G. H. Zhu, G. Joshi, D. Z. Wang, J. Yang, A. J. Muto, M. Y. Tang, J. Klatsky, S. Song, M. S. Dresselhaus, G. Chen and Z. F. Ren, *Applied Physics Letters*, 2008, 93, 193121.
4. Yanzhong Pei, Xiaoya Shi, Aaron LaLonde, HengWang, Lidong Chen and G. Jeffrey Snyder, *Nature*, 2011,473, 66-69, DOI: 10.1038/nature09996.
5. Y. Pei, H. Wang and G. Snyder, *Advanced Materials*, 2012, 24, 6125-6135.
6. M. Zhou, Z. M. Gibbs, H. Wang, Y. Han, C. Xin, L. Li and G. J. Snyder, *Physical Chemistry Chemical Physics*, 2014, 16, 20741-20748.
7. Lipeng Hu, Tiejun Zhu, Xiaohua Liu, and Xinbing Zhao, *Advanced Functional Materials*, 2014, 24(33): 5211-5218. DOI: 10.1002/adfm.201400474.
8. Li-Peng Hu, Tiejun Zhu, Ya-Guang Wang, Han-Hui Xie, Zhao-Jun Xu and Xin-Bing Zhao, *NPG Asia Materials*, 2014, 6(2): e88. DOI: 10.1038/am.2013.86.
9. Joseph P. Heremans, Vladimir Jovovic, Eric S. Toberer, Ali Saramat, Ken Kurosaki, and S. Y. Anek Charoenphakdee, G. Jeffrey Snyder, 2008, *Science,*321(5888): 554-557. DOI: 10.1126/science.1159725.
10. J.-J. Shen, T.-J. Zhu, X.-B. Zhao, S.-N. Zhang, S.-H. Yang and Z.-Z. Yin, *Energy & Environmental Science*, 2010, 3, 1519.
11. A. L. Yanzhong Pei, Shiho Iwanaga and G. Jeffrey Snyder, *Energy & Environmental Science*, 2011, 4(6): 2085-2089. DOI: 10.1039/c0ee00456a.
12. L. D. Zhao, S. H. Lo, Y. Zhang, H. Sun, G. Tan, C. Uher, C. Wolverton, V. P. Dravid and M. G. Kanatzidis, *Nature*, 2014, 508, 373-377.
13. M. Peters and L. McNeil, *Physical Review B*, 1990, 41, 5893.
14. S. Sassi, C. Candolfi, J. B. Vaney, V. Ohorodniichuk, P. Masschelein, A. Dauscher and B. Lenoir, *Applied Physics Letters*, 2014, 104,212105.
15. C.-L. Chen, H. Wang, Y.-Y. Chen, T. Day and G. J. Snyder, *Journal of Materials Chemistry A*, 2014, 2, 11171.
16. F. Lotgering, *Journal of Inorganic and Nuclear Chemistry*, 1959, 9, 113-123.
17. K. Kutorasinski, B. Wiendlocha, S. Kaprzyk and J. Tobola, *Physical Review B*, 2015, 91, 205201.
18. J. Carrete, N. Mingo and S. Curtarolo, *Applied Physics Letters*, 2014, 105, 101907.
19. D. Morelli, V. Jovovic and J. Heremans, *Phys. Rev. Lett.*, 2008, 101, 035901.
20. M. D. Nielsen, V. Ozolins and J. P. Heremans, *Energy & Environmental Science*, 2013, 6, 570-578.
21. Y. Zhang, E. Skoug, J. Cain, V. Ozoliņš, D. Morelli and C. Wolverton, *Physical Review B*, 2012, 85, 054306.
22. S. Wang, J. Yang, T. Toll, J. Yang, W. Zhang and X. Tang, *Scientific reports*, 2015, 5,10136.
23. A. Pashinkin, A. Malkova, V. Fedorov and M. Mikhailova, *Inorganic Materials*, 2006, 42, 593-595.
24. K. Yamaguchi, K. Kameda, Y. Takeda and K. Itagaki, *Materials Transactions, JIM*, 1994, 35, 118-124.
25. T. Caillat, A. Borshchevsky and J. P. Fleurial, *Journal of applied physics*, 1996, 80, 4442-4449.
26. Leng, H. Q., Zhou, M., Zhao, J., Han, Y. M., & Li, L. F., *Journal of Electronic Material,* 2015*,* DOI :10.1007/s11664-015-4143-4.

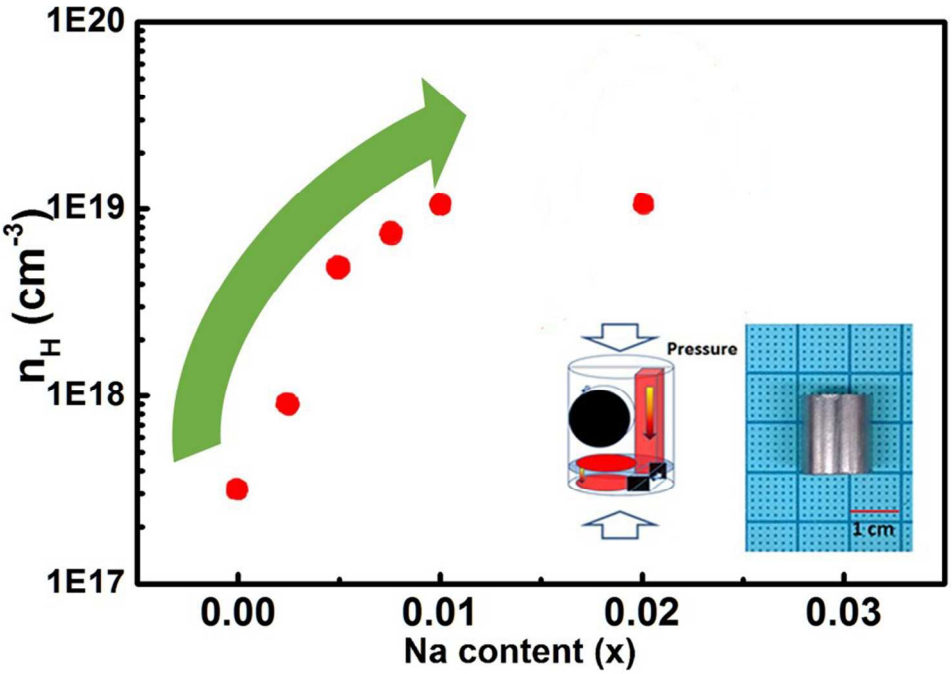

268x184mm (96 x 96 DPI)